PAPER

Iron-assisted ion beam patterning of Si(001) in the crystalline regime

New Journal of Physics
The open-access journal for physics

Iron-assisted ion beam patterning of Si(001) in the crystalline regime

Sven Macko[1,4], Jörg Grenzer[2], Frank Frost[3], Martin Engler[1], Dietmar Hirsch[3], Monika Fritzsche[2], Arndt Mücklich[2] and Thomas Michely[1,4]

[1] II. Physikalisches Institut, Universität zu Köln, Zülpicher Strasse 77, D-50937 Cologne, Germany
[2] Institute of Ion Beam Physics and Materials Research, Helmholtz-Zentrum Dresden-Rossendorf, PO Box 510119, D-01314 Dresden, Germany
[3] Leibniz-Institut für Oberflächenmodifizierung eV, Permoserstrasse 15, D-04318 Leipzig, Germany
E-mail: michely@ph2.uni-koeln.de and macko@ph2.uni-koeln.de

New Journal of Physics **14** (2012) 073003 (16pp)
Received 7 March 2012
Published 3 July 2012
Online at http://www.njp.org/
doi:10.1088/1367-2630/14/7/073003

Abstract. We present ion beam erosion experiments on Si(001) with simultaneous sputter co-deposition of steel at 660 K. At this temperature, the sample remains within the crystalline regime during ion exposure and pattern formation takes place by phase separation of Si and iron-silicide. After an ion fluence of $F \approx 5.9 \times 10^{21}$ ions m^{-2}, investigations by atomic force microscopy and scanning electron microscopy identify sponge, segmented wall and pillar patterns with high aspect ratios and heights of up to 200 nm. Grazing incidence x-ray diffraction and transmission electron microscopy reveal the structures to be composed of polycrystalline iron-silicide. The observed pattern formation is compared to that in the range of 140–440 K under otherwise identical conditions, where a thin amorphous layer forms due to ion bombardment.

[4] Author to whom any correspondence should be addressed.

Contents

1. Introduction

It is now well established that room-temperature pattern formation on Si surfaces due to low-energy ion beams (energies ranging from a few hundreds of eV to a few keV) requires co-deposition of additives [1–8], except at grazing angles $\vartheta > 50^\circ$ with respect to the surface normal [1, 3, 4, 9]. Since additives can hardly be avoided in ion erosion experiments and since their presence is not obvious in view of their low concentrations, the understanding of pattern formation was hampered by contradicting experimental results and lab-to-lab reproducibility problems in the past. The observed nanopattern formation is associated with a nonuniform distribution of the additives in the thin surface layer, which is amorphized under the ion beam. For the well-studied cases of Fe and Mo additives, it is invariably found that the additives accumulate at the elevations of the patterns, in the ripple crests or the dots [2–4, 10]. The reduced erosion rate of the areas rich in additives is thought to amplify the pattern amplitude [2–4], while the nonuniform distribution of the additives is speculated to result from ion-beam-induced phase separation [3] or from flux inhomogeneities triggered by height fluctuations [2]. The low-energy ion-beam-induced nanopatterns are usually relatively shallow with amplitudes of the order of 10 nm and characteristic separations well below 100 nm; see, e.g., [2–4, 10].

Pattern formation induced by additives during ion beam exposure of surfaces had already attracted considerable attention in a first wave of studies following the seminal work of Wehner and Hajicek [11] in the eighties and nineties of the last century. However, these early pattern observations relate to much coarser structures with lateral dimensions of several hundreds of nm to μm and with high aspect ratios. The resulting patterns are usually well described as a topography of more or less dense sputter cones. In the formation of such patterns, usually elevated temperatures are invoked [10, 12–14]. Also in the cone patterns the additive is found to be concentrated at the cone tops. Specifically for the case of co-deposition during ion exposure of Si at elevated temperatures, silicide formation was observed in the upper parts of the cones [10, 13, 15].

The question arises: how far are the ‘modern’ ion beam nanopatterns and the ‘old’ sputter cone topographies linked in their nature and what makes them distinct from each other? One way to answer this question is through temperature-dependent studies, which are rare to date [14, 15]. To contribute to this ongoing effort, we focus in this study on Fe-assisted pattern formation on Si(001) and compare experimental results obtained at 660 K substrate temperature to the results we obtained under exactly identical conditions for the same system, but at 440 K and below.

We will find that by increasing the temperature the morphology dramatically changes as soon as Si remains crystalline during ion beam erosion. Instead of amorphous or nanocrystalline

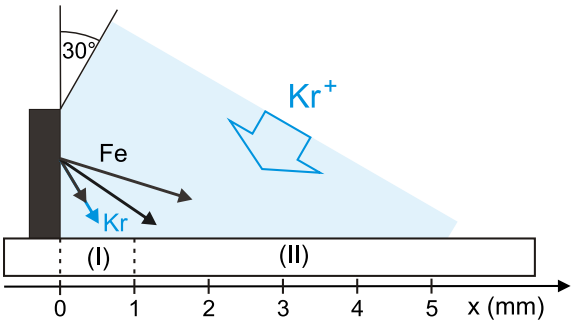

Figure 1. Sketch of the sputter co-deposition setup (see text).

areas of enhanced Fe concentration, now polycrystalline iron silicides are formed. Instead of relatively smooth ripples and dots ('modern' ion beam nanopatterns), now high-aspect-ratio structures (sponges, pillars and walls) are observed that come close to the 'old' sputter cone topographies. At such elevated temperatures, pattern formation involves diffusion, nucleation and phase separation. For the pattern formation as such, geometric effects are only of marginal importance, while we could show them to be of great importance at low temperatures [2]. However, in view of pattern symmetry and additive distribution, similarities are also found that will be highlighted. We note that the understanding of impurity-assisted ion beam pattern formation at elevated temperatures is not only of academic interest. The large variety of high-aspect-ratio surface structures and patterns has potential applications, and a better understanding of their formation mechanisms will certainly increase our ability to tailor functional surfaces. Ion beam patterned surfaces display a minimized reflectivity and are thus promising to optimize solar cells (e.g. 'black' silicon) [16–18] or optoelectronic devices [19, 20]. Structures such as arrays of cones and pillars oriented upstanding to the Si substrate were found to be an ideal material for enhancing the performance of thermoelectric generators [21]. Moreover, nanostructured silicon was identified not only as a bio-compatible material supporting cell and apatite growth (the latter being a major component of bone tissue) [22, 23] but also as a promising material for small sensitive sensors [24].

2. Experiment

For the sputter co-deposition experiment, a piece of stainless steel (Fe 84% and Cr 13%) was mounted on the Si(001) sample as shown in figure 1. For brevity, we will refer to the co-deposited material as 'Fe', in the text and figures. A 2 keV Kr^+ ion beam with a full-width at half-maximum of ≈1 mm was then scanned over the sample and steel target, resulting in simultaneous erosion and metal deposition on the Si sample. The time-averaged flux of primary Kr^+ ions arriving at the Si sample was $\Phi_{Kr} = 3.4 \times 10^{17}$ ions m^{-2} s^{-1}. Within the entire scan area, the uniformity of the ion flux was better than 10%; within the area 0.5 mm away from the edges of the scan area, it was better than 5% as measured by a movable Faraday cup. Using the cup, prior to and after each experiment, the ion flux was checked. The ion fluence to the sample was $F = 5.9 \times 10^{21}$ ions m^{-2}. Due to differential pumping during ion exposure, the working pressure was below 1×10^{-7} mbar. After ion exposure, the pressure dropped quickly into the 10^{-11} mbar range.

After preparation the Si sample topography was analyzed depending on the distance x in the normal direction to the steel plate (compare figure 1) by *ex situ* atomic force microscopy (AFM) and scanning electron microscopy (SEM). The structure of surface patterns was studied by transmission electron microscopy (TEM). For the cross-sectional imaging a Titan 80–300 microscope was used, equipped with a field emission gun working at 300 keV and an image corrector to minimize spherical aberrations. Within the TEM, the chemical composition was analyzed by energy dispersive x-ray spectroscopy (EDX). For the TEM lamellae preparation, a combination of a focused ion beam (FIB) and an SEM was used (Zeiss NVision 40). This instrument uses Ga^+ ions to cut out the TEM lamellae. To protect the surface from Ga^+ irradiation a carbon layer was deposited on the structures of interest using a gas injection system and the scanning electron microscope. The lift-out of this lamellae was done *in situ* and for thinning the FIB was operated at 5 keV. The crystal lattice structure was analyzed by grazing incidence x-ray diffraction (GI-XRD). The measurements were made by an optimized x-ray laboratory setup using Cu-K_α radiation and a beam size of 200 μm. The scattered x-ray signal was detected using a position-sensitive detector.

As a prerequisite for the discussion of the co-sputter deposition experiment at 660 K, we recall some basic consequences of the deposition geometry already presented in a previous publication [1], where this geometry was used for room-temperature sputter co-deposition. As shown in figure 1, the primary ion beam hits the Si sample under an angle $\vartheta = 30^\circ$ with respect to the sample surface normal. At the same time the stainless steel target is hit at an angle $\vartheta_t = 60^\circ$ with respect to the local surface normal of the target by Kr^+ ions. Sputtered Fe and Cr atoms leave the target with a broad angular distribution and the most probable emission angle of $\vartheta_t \approx 37^\circ$ (compare figures 6(a) and (c) of [1] for the angular and energy distributions). They rise to a substantial flux of arriving additive atoms on the sample. The additive atom flux diminishes with increasing normal distance x from the stainless steel plate. In addition, primary Kr^+ are scattered at the target surface. They leave the target surface with substantial energy, a rather narrow angular distribution and the most probable emission angle $\vartheta_t = 68^\circ$ (compare figures 6(b) and (c) of [1] for the angular and energy distributions). Consequently, in the region adjacent to the stainless steel plate with $0 \leqslant x \leqslant 1$ mm and indicated as (I) in figure 1, fluxes of scattered Kr atoms and sputtered additive atoms arrive at the sample, in addition to the primary Kr^+. In the region indicated as (II) in figure 1 with $x > 1$ mm, the flux of Kr scattered at the target is absent.

3. Results

In the first part of the results section, we characterize the pattern caused by Fe co-deposition during ion erosion at 660 K by AFM and STM as a function of the distance x from the steel plate (compare figure 1).

Figures 2(a)–(f) are a sequence of AFM topographs of the morphology with increasing x-coordinate. At first glance, it seems obvious that starting from a smooth surface (figure 2(a)) pointed elevations nucleate already close to the steel plate (figure 2(b)), become denser with increasing x (figure 2(c)) and then gradually decrease in density and height (figures 2(d) and (e)) until a rather smooth surface is reestablished (figure 2(f)). The pointed elevations are named pillars in the following. The maximum pillar height increases from about 150 nm (figure 2(b)) to 185 nm (figure 2(c)), then decreases gradually to 155 nm (figure 2(d)) and finally to 105 nm in figure 2(e). The roughness σ of the base level, on which the pillars grow, is rather low.

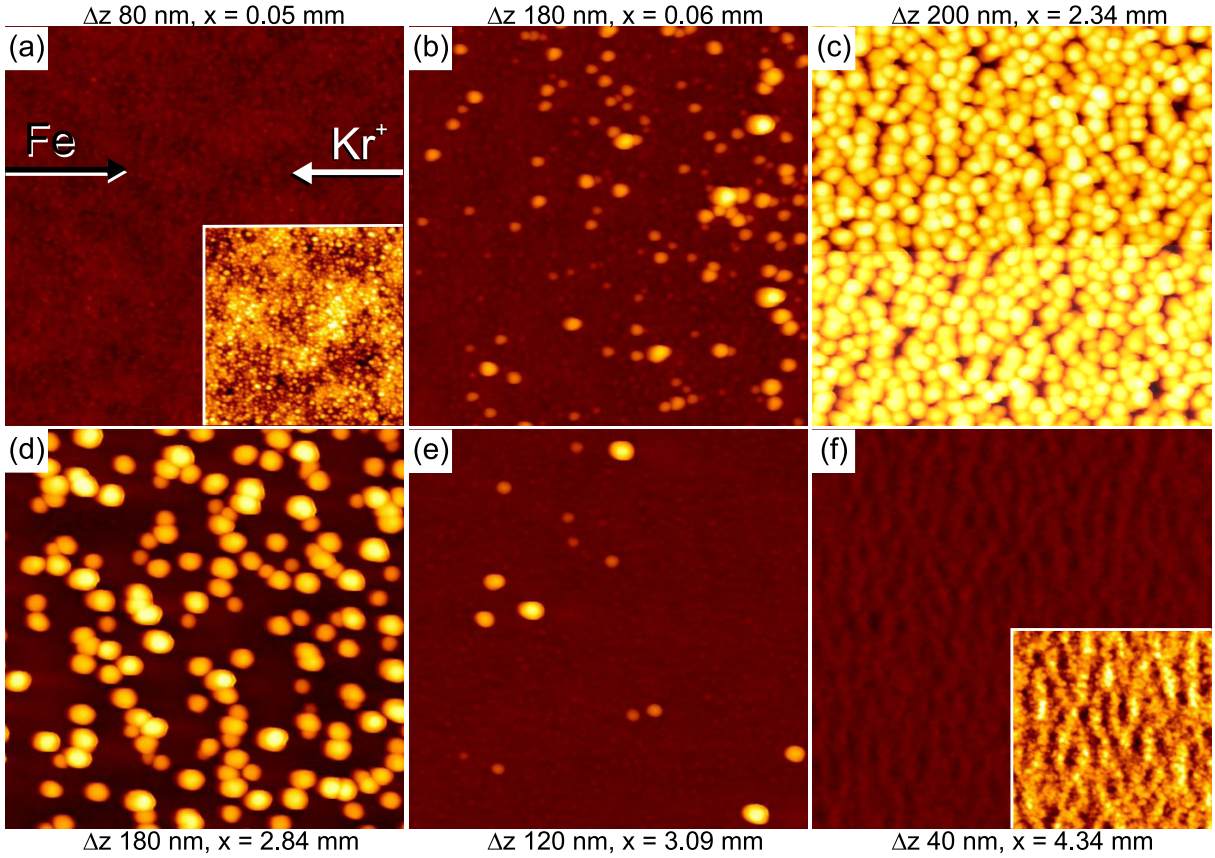

Figure 2. AFM images of Si(001) after sputter co-deposition at 660 K depending on the distance x from the steel plate. The projection of the incoming directions of Kr^+ and Fe on the surface for all images is indicated in panel (a) by the white and black arrows, respectively. The x-coordinate and the height range Δz spanned by the color scale are indicated above (a)–(c) or below (d)–(f) each topograph. The topograph size is $2\,\mu m \times 2\,\mu m$. Insets in panels (a) and (f) show the according surface with optimized contrast with a size of $1\,\mu m \times 1\,\mu m$.

It decreases from $\sigma \approx 3$ nm at $x \approx 0.05$ mm (figures 2(a) and (b)) gradually via $\sigma \approx 2$ nm at $x \approx 3$ mm (figures 2(d) and (e)) to $\sigma \approx 1.0$ nm at $x = 4.34$ mm (figure 2(f)). Due to the high density of pillars it was not possible to measure the roughness of the base level in figure 2(c). The background is rather smooth in view of the pillar heights. It is of the same magnitude as that obtained by ion beam erosion under identical conditions at 660 K, but without Fe co-sputtering. The inset of figure 2(a) with optimized contrast highlights the grainy nature of the background. In figure 2(f) a smooth, poorly ordered ripple pattern with a wavelength $\lambda = 150$ nm becomes visible, which is highlighted by the enhanced contrast of the inset. It gradually emerges for $x \geqslant 3$ mm.[5]

Although the sequence of AFM images presented in figure 2 seems to display a conclusive morphological evolution as a function of the x-coordinate, the information is not complete.

[5] For some of the x-coordinate values that could not be measured by AFM the background displays substantial roughness. Compare figures 6(a) and (b) and the related discussion.

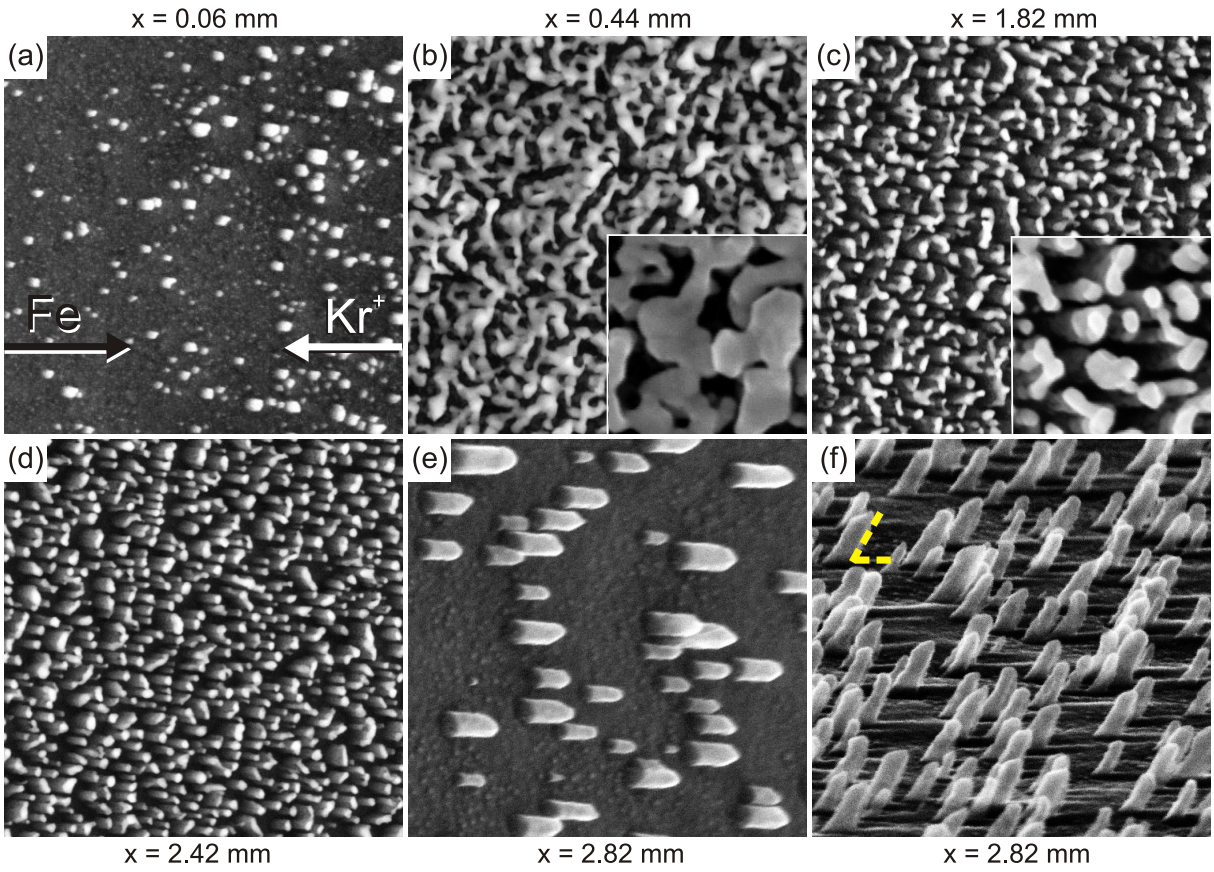

Figure 3. Top (a)–(e) and sideview (f) SEM images after sputter co-deposition at 660 K on Si(001) as a function of distance x from the steel target. The projection of the incoming directions of Kr^+ and Fe on the surface for all images is indicated in (a) by the white and black arrows, respectively. The x-coordinate is indicated above (a)–(c) or below (d)–(f) each topograph. The image width for (a)–(d) is 2 μm and for (e) and (f) it is 1 μm. Note that the top view in (e) is slightly tilted away from the observer at the right-hand side to make pillars better visible. The size of insets is 400 nm × 400 nm. The dashed yellow lines in (f) indicate an angle of 60°, i.e. the pillars are oriented 30° with respect to the surface normal.

AFM imaging free of dominating tip artifacts was impossible in the range 0.1 mm $\leqslant x \leqslant$ 2.2 mm. A rough surface with very dense high-aspect-ratio features could be identified, but a proper analysis of the surface morphology in this range requires SEM imaging. Figures 3(a)–(e) are a sequence of top view SEM images of the morphology with increasing x-coordinate. Figures 3(a) and (d) match in x-position rather well to figures 2(b) and (c), respectively and are thus complementary views of the same morphological situation. The comparison of figures 3(d) and 2(c) makes plain that the AFM imaging considerably overestimates the lateral dimension of the pillars due to AFM-tip and pillar convolution. Two additional pieces of key information are encoded in the sequence of figure 3: (i) in the range 0.1 mm $\leqslant x \leqslant$ 1 mm a sponge structure is present rather than pillars, i.e. the basic morphological elements are cavities within a percolated elevated network (compare figure 3(b)). Globally, the sponge displays little anisotropy linked

to the directions of the impinging Kr^+ or Fe atoms. The inset of figure 3(b) highlights that the sponge displays a faceted structure suggesting a polycrystalline nature of the sponge. (ii) The ion beam imprints its direction on the pattern for $x \geqslant 1$ mm. The sideview SEM topograph of figure 3(f) shows unambiguously that the pillars are oriented precisely in the direction of the impinging ion beam (an angle of 60° is indicated by the yellow dashed lines). It is also clearly visible in figures 3(c) (see also the inset in (c)), (d) and (e) that the top of the elevated structures is always to the right of their root point, consistent with their alignment along the direction of the incoming ion beam. We note that such an alignment of high-aspect-ratio structures formed during ion exposure with co-deposition has been noted consistently in previous investigations [13–15].

A number of additional features apparent in the SEM images need to be mentioned. Firstly, considering the sequence of images from figures 3(b)–(e) it is obvious that the high-aspect-ratio structures transform from a percolated network in figure 3(b) within the range $0.1\,\text{mm} \leqslant x \leqslant 1\,\text{mm}$ to a pattern of disconnected wall segments in figure 3(c) within the range $1\,\text{mm} \leqslant x \leqslant 2\,\text{mm}$ to a pattern of pillars in figures 3(d) and (e) within the range $2\,\text{mm} \leqslant x \leqslant 3\,\text{mm}$, of which the pillar density decreases with x. The area fraction of elevated surface parts thus decreases with the x-coordinate. Secondly, the SEM images allow one to determine the shape of the pillars. The single pillars shown in figures 3(e) and (f) have an average diameter of 45 nm and an average height of 170 nm. The tip apex is symmetric with respect to the x-direction (compare figure 3(e)) but asymmetric in the side view of figure 3(f), with an apex angle of about 100° in both cases. For smaller x-coordinate values the pillars increase their aspect ratio with an average diameter down to 30 nm and an average height of 180 nm. Also their tip apex flattens out.

Visual inspection of the sample after sputter co-deposition shows a black surface in the highly corrugated areas displaying sponge, wall and dense pillar structures. The enhanced absorption of the sample is consistent with the observations of Zhou *et al* [10], who found the same for cone arrays after Fe sputter co-deposition. The temperature of sputter co-deposition in their work was about 800 K, due to ion-induced heating under high ion current conditions. The reduced reflectivity can be attributed to the moth-eye effect [16, 18, 25]: the high-aspect-ratio pattern with a lateral length scale smaller than the wavelength of light gives rise to a continuous change of the index of refraction and thereby reflection is suppressed.

To uncover the crystalline structure and composition of the ion beam patterned surface, we conducted GI-XRD and TEM experiments. Prior to the x-ray diffraction measurements, the critical angle of total external reflection of the samples was determined to be $\alpha_c = 0.27°$. The measurements were carried out slightly below that value, at $\alpha_i = 0.20°$. Under these conditions the evanescent x-ray wave propagates predominantly at the sample surface so that it is highly sensitive to the surface structure and at the same time less sensitive to bulk scattering.

As a reference we first analyzed a sample patterned at 440 K under otherwise identical conditions by GI-XRD. Besides the signal of the Si bulk, no other crystalline structures could be detected. A different situation presents itself for the sample treated at 660 K. Figure 4 shows GI-XRD results, where an additional FeSi diffraction pattern is displayed after removing the background. The black dots show the positions and the relative intensity of a theoretical cubic ε-FeSi structure with a lattice constant of 4.488 Å in a B20 configuration. At least six of the most intense FeSi peaks could be observed. From the measured intensity distribution a powder-like phase and an average crystallite size of about 20 nm could be estimated.

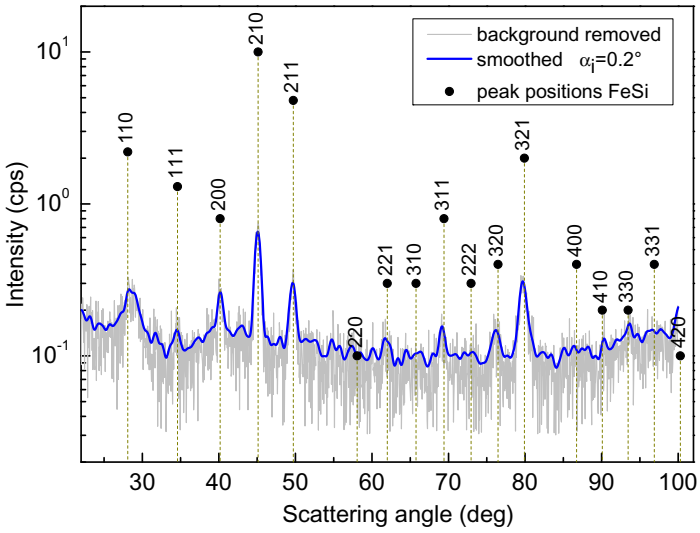

Figure 4. GI-XRD diffraction curve. The blue intensity curve over the scattering angle shows the smoothed x-ray scattering intensity after removal of the background signal (grey). Several characteristic peak positions of ϵ-FeSi are marked within the diagram (black dots).

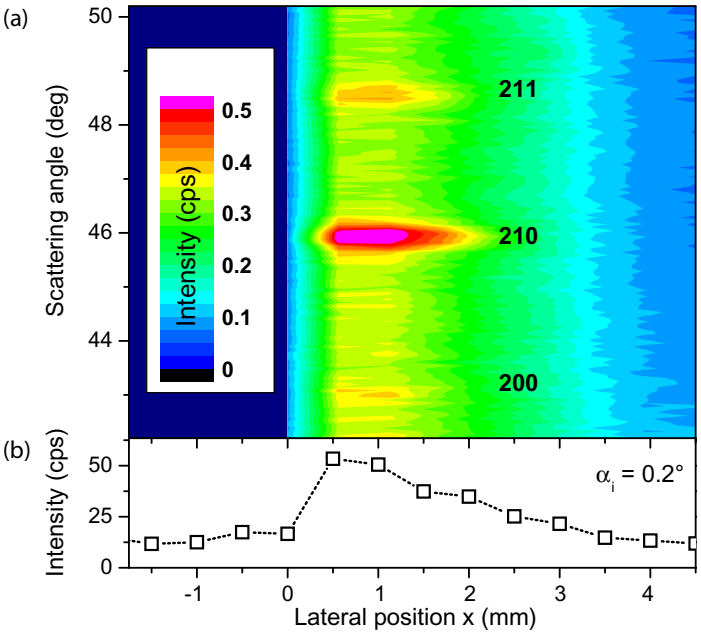

Figure 5. (a) Spatially resolved GI-XRD signal. (b) Intensity curve of the (210) peak depending on the position x. Position $x = 0$ mm corresponds to the position of the steel plate.

As the Fe content changes with the distance x relative to the steel target we additionally carried out a position-dependent diffraction measurement along x. Thereby the x-ray beam crossed the patterned area parallel to the steel plate. The results are presented in figure 5(a)

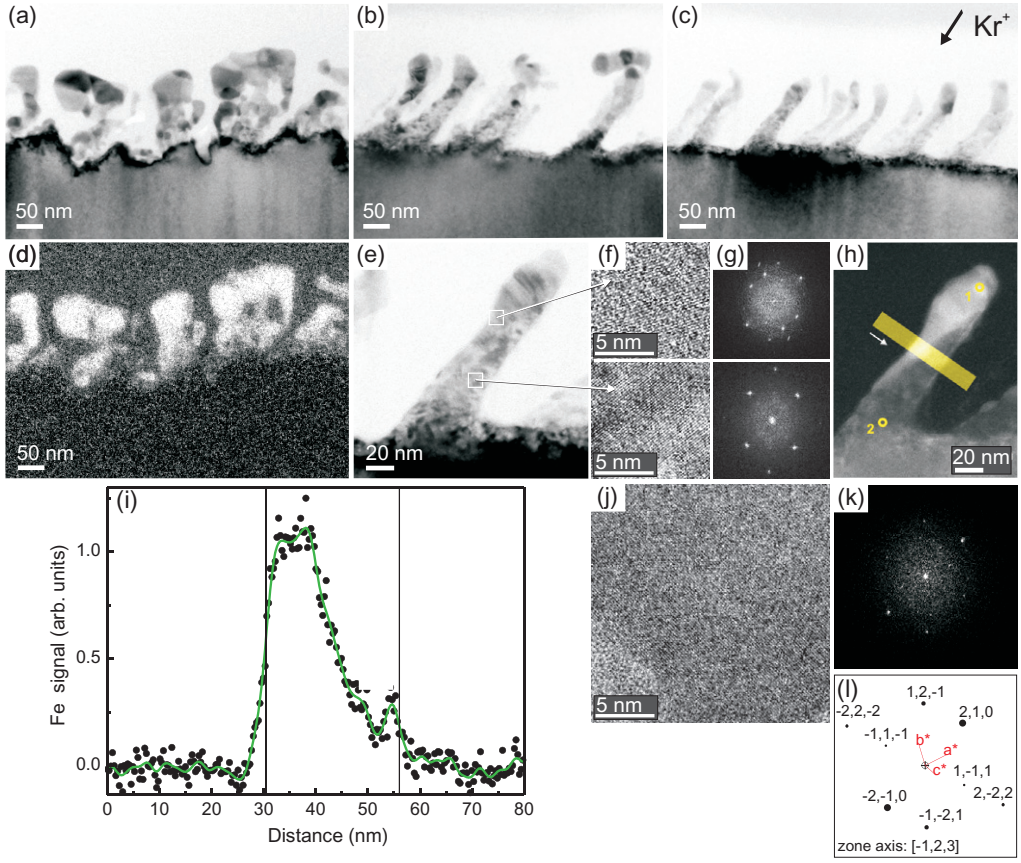

Figure 6. TEM analysis with TEM imaging positions at (a) $x = 0.45$ mm, (b) $x = 1.80$ mm and (c) $x = 2.45$ mm. (d) Image subtraction of energy-filtered TEM measurements: bright regions represent a high Fe content (see text), the position x corresponds to (a). (e) TEM image of a nanopillar at $x = 2.45$ mm. (f) High-resolution TEM images of areas bordered in (e). (g) FFT analysis of regions displayed in (f). (h) Energy-filtered TEM measurement of the pillar presented in (e). (i) EDX linescan across the pillar along the yellow line in (h). The vertical lines indicate the border of the pillar. (j) High-resolution TEM image of the position $x = 0.45$ mm. (k) FFT of (j). (l) Expected FFT reflexes for FeSi.

where the intensities of the (211), (210) and (200) FeSi peaks depending on x are clearly visible. Additionally, figure 5(b) shows the integrated intensity of the (210) peak, the most pronounced peak, depending on x. A maximum in intensity is found in the Fe-rich range of the sponge-like structure $0.2\,\text{mm} \leqslant x \leqslant 1\,\text{mm}$. As the sponge transforms to the wall structure, the intensity decreases with increasing x just as the fraction of the bare substrate increases (compare figures 3(b)–(d)). At a distance $x \approx 2.4$ mm the diffraction intensity falls below the detection limit.

To get a better understanding of the Fe distribution within the structures, TEM measurements were made. Figure 6(a) shows a TEM brightfield image of a lamella cut out by FIB at the position $x \approx 0.45$ mm displaying a sideview of the sponge-like structure. The features are composed of patches differing in brightness, which is an indication of differently

oriented crystallites. A coarse substrate below the sponge-like features is visible. Separated pillars appear in figures 6(b) and (c) at positions $x \approx 1.80$ mm and $x \approx 2.45$ mm, respectively. As already presented in the SEM images of figure 3(f) the pillars point in the direction of the incoming Kr^+ beam.

Figure 6(d) is the result of an image subtraction of two energy-filtered TEM images recorded with electron energies just below and above the excitation energy (Fe-$M_{2,3}$ edge) of Fe. Thus the bright areas in the subtracted image represent a high Fe content. As figures 6(a) and (d) are recorded at the same sample position, comparison of the images reveals the Fe to be distributed entirely within the sponge-like features. High-resolution TEM analysis (e.g. figure 6(j)) within the structures presented in figures 6(a) and (b) confirm an FeSi structure as found by GI-XRD measurements. The fast Fourier transform (FFT) in figure 6(k) shows a slightly distorted FeSi structure as compared with the expected spots in figure 6(l).

A TEM image of an isolated pillar at $x = 2.45$ mm is shown in figure 6(e). Again the patches of different brightness indicate differently oriented crystallites. Two areas are framed by white boxes. Within these areas high-resolution TEM images were recorded, which are presented in figure 6(f). Both areas show an ordered crystalline structure. The according FFT is displayed in figure 6(g). From the distance and orientation of the FFT spots the crystal lattice structure can be estimated. The FFT corresponding to the upper part of the pillar with well-defined spots has a rather complex structure and does not fit any common iron-silicide[6] structure, nor to pure Fe or Si. According data fits of the FFT spots suggest rather a tetragonal $FeSi_2$ or a distorted Fe_2Si structure but both assumptions should be viewed with caution. We note also that the simultaneous deposition of a small amount of Cr from the stainless steel target may have an effect on the structure of the silicide phase. The FFT analysis of the bottom part of the pillar shows spots of pure Si oriented in the substrate direction which is Si(001).

Figure 6(h) displays an energy filtered TEM image of the pillar shown in figure 6(e); again the bright regions represent areas with high Fe content. It is conspicuous here that the top of the pillar is Fe-rich while the bottom contains no significant amount of Fe. A straight border of the Fe-rich pillar region is visible. It crosses the pillar diagonally from the lower part of the pillar on the Fe influx facing side to the upper part of the pillar on the Fe influx averted side. EDX was conducted at the top and bottom of the pillar (points 1 and 2, respectively) underlining once again that the Fe content is considerable higher in the region at the top of the pillar compared to the bottom of the pillar (EDX spectra are not shown here).

Figure 6(i) shows an EDX linescan along the yellow line in figure 6(h) in the direction of the indicated white arrow. It is evident that there is a sharp border changing from high Fe content to low Fe content from the Fe influx facing side of the pillar to the Fe influx averted side, respectively. Looking more precisely at the EDX linescan in figure 6(i), another yet smaller Fe peak is present at the Fe influx averted side. Consequently, this Fe must be a consequence of the redeposition of Fe sputtered from neighboring pillars.

Consistent with our TEM observations, we find that the Si matrix and the surface layer remain crystalline at 660 K. Low-energy electron diffraction conducted after ion erosion at 660 K under identical conditions, but without Fe sputter co-deposition, displays the characteristic (2×1) spots of the Si(001) dimer reconstruction as shown in figure 7. At this temperature the spots are still broad and diffuse, indicative of small-sized diffraction domains

[6] Please note that, in the following, we use the term 'iron-silicide' as a generic term for all possible iron-silicide compositions, while 'FeSi' stands for the specific iron-silicide with an Fe to Si proportion of 1 : 1.

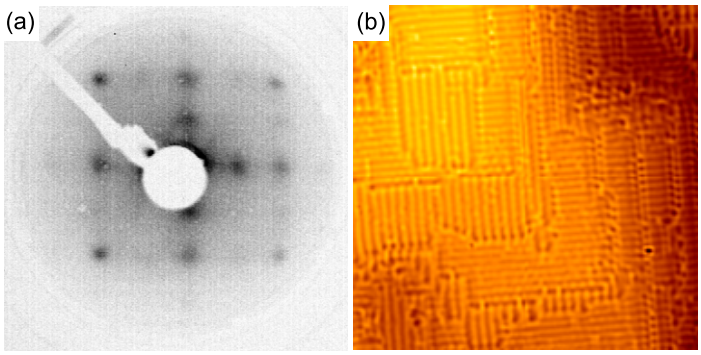

Figure 7. (a) Low-energy electron diffraction pattern of Si(001) at 66 eV after 2 keV Kr^+ ion beam erosion in the absence of Fe sputter co-deposition, but under otherwise identical conditions. (b) Laplace filtered STM topograph of the same surface displaying crystalline terraces and the (2×1) dimer row reconstruction of Si(001). The image size is 30 nm × 30 nm.

and some disorder in the surface layer. This picture is substantiated by the STM topograph shown in figure 7(b). It displays a clear, but defective, step and terrace structure after a 660 K ion erosion.

4. Discussion

Room-temperature pattern formation during ion beam erosion and in the presence of Fe impurities was shown to be due to an inhomogeneous Fe distribution on the surface through ion-induced phase separation or height fluctuations or both [2, 3]. As the erosion rate of the amorphous iron silicide is lower than that of pure Si, height differences evolve with the silicide found at the pattern elevations and the Si in the depressions. To a first approximation, the same global mechanism can be considered to be operative at 660 K, too.

However, we observe striking differences in pattern formation by Fe co-deposition during ion erosion of Si(001) when conducted at 660 and 440 K (or below). These differences are key to a deeper understanding of the respective pattern formation mechanism. Figure 8 compares schematically the morphology at 660 K to those resulting from co-deposition during sputtering in the temperature range of 140–440 K. The latter are described in detail in [2]. Roughly speaking, we observe four key differences: (i) at 660 K the sample is polycrystalline (including the Fe-rich volume), while at 440 K due to the ion beam a thin amorphous layer forms on top of the single crystal substrate. (ii) At 660 K the Fe-rich layer has for most x-values a thickness above 150 nm, while at 440 K it is limited to the amorphous layer with a thickness of about 8 nm. (iii) Most strikingly, in region (I) for $x \leqslant 1$ mm at 660 K a sponge structure with thickness well above 150 nm (up to 200 nm) results, while at 440 K the same region remains smooth with a roughness $\sigma \leqslant 0.4$ nm and a faint hole pattern. (iv) At 660 K the pattern amplitude and feature aspect ratios are strongly enhanced.

Still, there are clear similarities between the two situations of co-deposition during ion erosion: (a) As far as we can tell, for both temperatures Fe is accumulated in the elevated parts of the patterns. (b) The patterns gradually fade in amplitude as well as in area fraction of the elevated pattern parts with increasing x-coordinate. (c) The sequences of patterns display similar

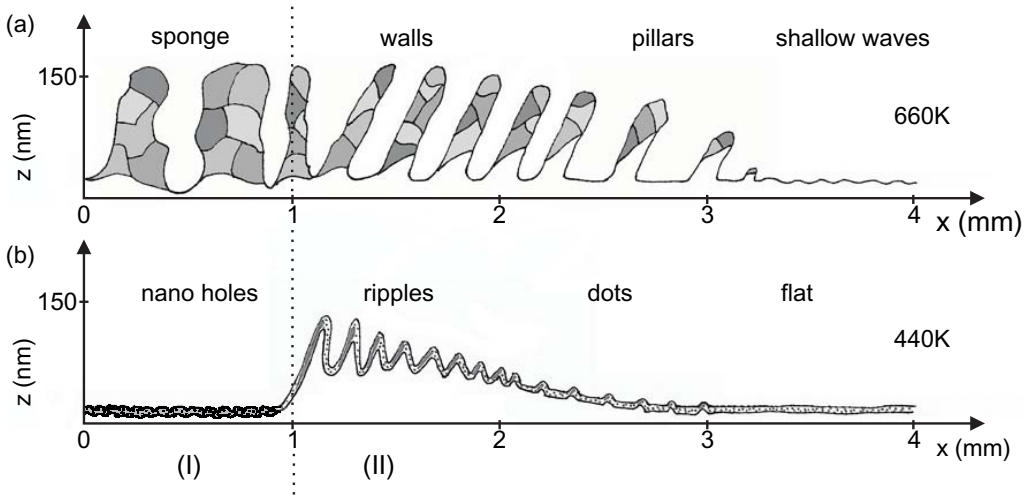

Figure 8. Schematic sketch of the morphology after Fe co-deposition during ion exposure as a function of the distance x to the steel plate at temperatures $T = 440$ K and $T = 660$ K.

topologies as a function of the x-coordinate. For $x \leqslant 1$ mm the patterns are almost isotropic and characterized by depressions in a connected structure of larger height. For 1 mm $\leqslant x \leqslant 2$ mm segmented ripples or segmented walls are observed, with their ridges preferentially normal to the x-axis (less pronounced at 660 K), which gradually decay to pillars or dots for 2 mm $\leqslant x \leqslant$ 3.1 mm until the pattern (largely) vanishes for $x \geqslant 3.1$ mm. (d) In both cases the patterns in region (II) with $x \geqslant 1$ mm are oriented with respect to the ion beam direction. This is obvious for 660 K, but also visible for the 440 K case (compare figures 5(d), (e) and 8(a) of [2]).

We focus first on the grossly different appearance of patterns in region (I), i.e. on difference (iii). The 150 nm thickness of the coalesced ϵ-FeSi layer in region (I) at 660 K is much larger than the range of the 2 keV Kr^+ ions, which is of the order of 8 nm. This implies immediately that bulk thermal diffusion of the arriving Fe atoms takes place at 660 K. The fact that at 660 K Si remains crystalline during ion erosion in the absence of Fe co-deposition implies that, at 660 K, recrystallization within the single-ion impact amorphized pockets takes place on a sufficiently fast time scale with respect to the experimental one set by the ion flux. The crevices in the Si substrate at the bottom of the sponge structure—locations ions are unable to reach simply due to geometry—also signify that Si surface diffusion is present (compare figure 6(a)). Driven by the Fe concentration gradient resulting from Fe arriving at the elevations, Si moves up to match the 1 : 1 stoichiometry of ϵ-FeSi. As the Si bottom of the sponge structure 150 nm below the surface cannot be reached by ions, the height of the sponge pattern is not related to ion beam effects, but to diffusion. The same conclusion holds also for the lateral length scale of the sponge pattern: knowing that at 660 K thermal diffusion is, by far, more efficient than ion-beam-induced diffusion renders the relevance of the latter for pattern length scale selection implausible.

Therefore thermal diffusion—rather than ion-induced diffusion—dominates phase separation into Si and ϵ-FeSi, the silicide with the highest enthalpy of formation [26]. It appears that the phase separation is by nucleation for $x \approx 0.05$ mm, where the flux of arriving sputtered

Fe atoms is still very small[7] (compare figures 2(b) and 3(a)). The same appears to hold for large $x \approx 3$ mm, where figures 2(d) and (e) as well as figure 3(e) display isolated pillars resulting from a nucleation process. In between, where the flux of arriving Fe is high, spinodal decomposition is likely to take place. The decreasing areal coverage of ϵ-FeSi with increasing x-coordinate indicates the decreasing amount of arriving Fe. In conclusion, the vertical as well as the lateral pattern length scales observed are largely set by thermal diffusion rather than ion beam effects.

Why is the situation at 440 K so different, specifically in region (I)? Globally, this difference is due to the absence of thermal diffusion and the absence of thermally driven phase separation at 440 K and below. The absence of thermal diffusion normal to the surface confines Fe incorporation and silicide formation to the thin ion beam amorphized layer of about 8 nm. For the same reason, only smooth variations of Fe concentration and height form the pattern, rather than sharp boundaries of crystalline phases. Still it is striking that at 440 K in region (I) no high-aspect-ratio features evolve, while they form in region (II). Considering the similar topology of the patterns formed at 440 and 660 K it appears plausible that the faint pattern of small and shallow holes observed at 440 K in region (I) indicates already the tendency for phase separation of the Fe–Si system, with the holes being richer in Si (as pure Si erodes faster, compare table 1 of [2]).

In [2], we demonstrated in controlled co-evaporation experiments that the relative directions of the impinging ion and additive fluxes are of great importance for pattern formation in the absence of thermal diffusion. Specifically, a small angle α between the two beams tends to hamper pattern evolution, while a large one fosters it. In this view, the scattered energetic Kr impinging in region (I) from the same direction onto the substrate as the Fe is efficiently damping phase separation and pattern build-up.

We could also speculate that it is not the scattered energetic Kr which damps pattern formation in region (I), but simply the fact that the stoichiometry in region (I) comes close to that of a stable iron silicide. In this case, there is a uniform iron silicide phase and no phase separation is possible. This conclusion holds also for ion-induced phase separation. Additional controlled co-evaporation experiments in this direction are certainly desirable, and the above speculation would gain support if for high impurity/flux ratios the absence of patterns could be observed.

With the preceding discussion, also the other striking differences already listed above between pattern formation at 660 and at 440 K can be explained: the onset of thermal diffusion of Fe and Si as well as their efficient reaction make understandable (i) the crystallinity of Si and the silicides at 660 K and the presence of an amorphous layer at 440 K, (ii) the large thickness of the ϵ-FeSi layer well beyond the ion range and (iv) the generally larger aspect ratio of the observed patterns enabled by the efficient phase separation resulting in pattern amplification through erosion rate differences.

Also the similarities between the patterns formed at 660 and 440 K are easily understood within the framework of the presented ideas: the accumulation of Fe in the elevations (a) is just a consequence of the reduced erosion rate of silicide or of regions with enhanced Fe concentration. The observation that the patterns gradually fade away with increasing x-coordinate (b) represents the simple fact that the Fe flux from the steel target fades away with increasing x-coordinate and thus the ability of the system to create regions with significant differences in erosion rate. The similar topologies (c) and similar orientation with respect to the

[7] Note that for geometric reasons at $x = 0$ mm the flux of arriving Fe atoms is zero.

ion beam (d) may be considered as resulting from rather similar boundary conditions in view of particle directions and geometry. Ion-beam-induced diffusion and thermal diffusion tend to act similarly, but with thermal diffusion present only at 660 K being much more efficient, giving rise to coarser patterns and higher aspect ratios.

Simple estimates for the arriving Fe flux indicate that it is highest in region (I) where the sponge pattern is observed at 660 K. Consistent with these estimates, the amount of ϵ-FeSi was found to be largest in region (I) (compare figure 5). However, at 440 K we found in region (I) a concentration c_{Fe} only half as large as that at the beginning of region (II). This apparent contradiction is resolved when considering that at 440 K the suppressed pattern build-up in region (I) causes efficient resputtering of the deposited Fe. In region (II), due to the large angle α between Fe flux and the Kr^+ ion beam, the Fe accumulates in the pattern flanks hardly illuminated by the ion beam. The Fe resputtering from the amorphous layer taking place at 440 K in region (I) is bypassed at 660 K by the rapid diffusion of excess Fe to the phase boundary between Si and ϵ-FeSi deep in the crystal and out of reach of the ion beam.

Why do our experiments display pillars with flanks parallel to the ion beam rather than the usually observed cones with opening angles of $\approx 30^\circ$ [6, 10, 13, 15]? From the fact that Zhou *et al* [10] observed cones for Fe sputter co-deposition at 800 K (although in a different sputter co-deposition geometry than that used here), where we observe pillars at 660 K, we are inclined to argue that the temperature is of decisive importance for the final shape and size of the structures formed. This is also plausible considering that thermal diffusion changes substantially with temperature. Similar to cones and pillars is not only the presence of crystalline silicide in the structures, but also the orientation towards the ion beam. The latter indicates that the ion beam is the dominating source of anisotropy in the system.

The fact that we are now able to draw a line from room-temperature nanopatterns, over pillars and walls discussed here, to cones formed at even higher temperatures indicates their common origin. The patterns differ substantially in lateral length scale and aspect ratio depending on whether they are just initiated by ion-induced mobility or whether thermal diffusion is also relevant (depending in magnitude on temperature).

Our TEM analysis of single pillars reveals that they display a sharp planar boundary between iron silicide and crystalline Si (compare figure 6(h)) normal to the direction of the impinging Fe flux. This planar boundary indicates that silicide formation is limited by the Fe supply, for $x \approx 2.5$ mm or larger. Although it was not unambiguously possible to distinguish whether the silicide in these pillars is a distorted Fe_2Si or a tetragonal $FeSi_2$, the latter Si-rich silicide appears to be the only one that makes sense in view of the limited Fe supply. We identified the smaller Fe peak in figure 6(i) associated with the Fe influx averted side of the pillar as shown in figure 6(h) to be due to redeposition of Fe sputtered from neighboring pillars. Also this Fe peak is certainly not associated with pure Fe but with a thin layer of $FeSi_2$. A close examination of figure 6(c) reveals that some pillars are bent upwards, towards the arriving Fe flux. Although this feature is not obvious in SEM (compare figures 3(c) and (d)), we have carefully checked that they do not arise from TEM sample preparation. A possible explanation arises from the fact that the pillars have an extended planar interface oriented almost along their axis. The thermal expansion coefficients of iron silicides [27] are about an order of magnitude larger compared to that of Si [28], which might give rise to a bi-metal effect. Upon cooldown from the growth temperature of 660 K, the strongly shrinking silicide would bend the pillar towards the Fe influx direction, as observed.

5. Conclusions

Fe impurity-induced ion beam pattern formation on Si(001) at elevated temperatures, where the Si matrix stays crystalline during erosion, is caused by phase separation through thermal diffusion. Depending on the ratio of the impurity atom to noble gas ion flux, the phase separation is by nucleation (low flux ratio) or spinodal decomposition (high flux ratio). High-aspect-ratio structures (pillars and walls) oriented in the direction of the ion beam are created. In the case of energetic particle impingement from two sides, the unique orientation is lost. For a sufficiently high Fe influx a sponge pattern forms. Nanoscale patterns formed at room temperature, at 660 K (pillars, walls and sponge patterns) and cone patterns formed at even higher temperatures are linked through silicide formation as the crucial step for pattern build-up. Silicide formation gives rise to laterally inhomogeneous erosion rates. Pattern formation remains largely temperature independent as long as the ion-beam-induced mobility exceeds thermal mobility. As soon as thermal mobility supersedes ion-induced mobility, pattern formation becomes strongly temperature dependent. High aspect ratios are achieved, as transport is no more limited to a vertical length scale of the order of the ion range. At 660 K bi-material pillars with sharp interfaces oriented primarily along the pillar axes can be formed. In view of their sensitivity to temperature and impurity to ion flux ratio, it appears that the impurity-induced ion beam patterns can be tuned in a wide morphological range to match the requirements for a wide variety of intended applications.

Acknowledgment

We gratefully acknowledge support from the Deutsche Forschungsgemeinschaft through Forschergruppe 845 and useful discussions with Hans Hofsäss.

References

[1] Macko S, Frost F, Ziberi B, Förster D F and Michely T 2010 *Nanotechnology* **21** 085301
[2] Macko S, Frost F, Engler M, Hirsch D, Höche T, Grenzer J and Michely T 2011 *New J. Phys.* **13** 073017
[3] Zhang K, Brötzmann M and Hofsäss H 2011 *New J. Phys.* **13** 013033
[4] Cornejo M, Ziberi B, Meinecke C, Hirsch D, Gerlach J W, Höche T, Frost F and Rauschenbach B 2011 *Appl. Phys.* A **102** 593
[5] Ozaydin G, Öczan A S, Wang Y, Ludwig K F, Zhou H, Headrick R L and Siddons D P 2005 *Appl. Phys. Lett.* **87** 163104
[6] Tanemura M, Yamauchi H, Yamane Y, Ohita T and Tanemura S 2004 *Nucl. Instrum. Methods Phys. Res.* B **215** 137
[7] Zhou J, Facsko S, Lu M and Möller W 2011 *J. Appl. Phys.* **109** 104315
[8] Madi C S, George H B and Aziz M J 2009 *J. Phys.: Condens. Matter* **21** 224010
[9] Madi C S and Aziz M J 2012 *Appl. Surf. Sci.* **258** 4112
[10] Zhou J, Hildebrandt M and Lu M 2011 *J. Appl. Phys.* **109** 053513
[11] Wehner G K and Hajicek D J 1971 *J. Appl. Phys.* **42** 1145
[12] Robinson R S and Rossnagel S M 1982 *J. Vac. Sci. Technol.* **21** 790
[13] Shang N G, Ma X L, Liu C P, Bello I and Lee S T 2010 *Phys. Status Solidi* A **207** 309
[14] Tanemura M, Yamauchi H, Yamane Y, Ohita T and Tanemura S 2006 *Surf. Sci.* **600** 3668
[15] Fujimoto Y, Nozu M and Okuyama F 1995 *J. Appl. Phys.* **77** 2725
[16] Sun C H, Jiang P and Jiang B 2008 *Appl. Phys. Lett.* **92** 061112

[17] Boden S A and Bagnall D M 2008 *Appl. Phys. Lett.* **93** 133108
[18] Hong S H, Bae B J, Han K S, Hong E J, Lee H and Choi K W 2009 *Electron. Mater. Lett.* **5** 39
[19] Wellner A, Palmer R E, Zheng J G, Kiely C J and Kolasinski K W 2002 *J. Appl. Phys.* **91** 3294
[20] Nassiopoulos A G, Grigoropoulos S, Gogolides E and Papadimitriou D 1995 *Appl. Phys. Lett.* **66** 1114
[21] Sökmen Ü, Fündling S, Merzsch S, Neumann R, Wehmann H H, Peiner E and Waag A 2010 *Microsyst. Technol.* **16** 863
[22] Mayne A H, Bayliss S C, Barr P, Tobin M and Buckberry L D 2000 *Phys. Status Solidi* A **182** 505
[23] Canham L T 1995 *Adv. Mater.* **7** 1033
[24] Lin V S Y, Motesharei K, Dancil K P S, Sailor M J and Ghadiri M R 1997 *Science* **278** 840
[25] Wilson S J and Hutley M C 1982 *Opt. Acta* **29** 993
[26] Predel B 1995 *Fe-Si (Iron-Silicon) (Springer Materials—The Landolt–Börnstein Database)* ed O Madelung (http://www.springermaterials.com)
[27] Vočadlo L, Knight K S, Price G D and Wood I G 2002 *Phys. Chem. Miner.* **29** 132
[28] Askeland D (ed) 1996 *Materialwissenschaften* (Heidelberg: Elsevier—Spektrum Akademischer Verlag)